UNCOVERing the extended strong lensing structures of Abell 2744 with the deepest JWST imaging

Furtak, L.J.; Zitrin, A.; Weaver, J.R.; Atek, H.; Bezanson, R.; Labbé, I.; ... ; Mowla, L.A.

Monthly Notices of the ROYAL ASTRONOMICAL SOCIETY

MNRAS **523,** 4568–4582 (2023)
Advance Access publication 2023 May 31

https://doi.org/10.1093/mnras/stad1627

UNCOVERing the extended strong lensing structures of Abell 2744 with the deepest *JWST* imaging

Lukas J. Furtak [1★] Adi Zitrin [1] John R. Weaver [2] Hakim Atek [3] Rachel Bezanson,[4] Ivo Labbé,[5] Katherine E. Whitaker,[2] Joel Leja [6,7,8] Sedona H. Price,[4] Gabriel B. Brammer,[9] Bingjie Wang(王冰洁) [6,7,8] Danilo Marchesini,[10] Richard Pan,[10] Pratika Dayal [11] Pieter van Dokkum,[12] Robert Feldmann,[13] Seiji Fujimoto [14,9] Marijn Franx,[15] Gourav Khullar,[4] Erica J. Nelson[16] and Lamiya A. Mowla[17]

Affiliations are listed at the end of the paper

Accepted 2023 May 25. Received 2023 May 25; in original form 2022 December 16

ABSTRACT

We present a new parametric lens model for the massive galaxy cluster Abell 2744 based on new ultra-deep *JWST* imaging taken in the framework of the UNCOVER program. These observations constitute the deepest *JWST* images of a lensing cluster to date, adding to existing deep *Hubble Space Telescope (HST)* images and the recent *JWST* Early Release Science and Director's Discretionary Time data taken for this field. The wide field of view of UNCOVER ($\sim$45 arcmin^2) extends beyond the cluster's well-studied central core and reveals a spectacular wealth of prominent lensed features around two massive cluster sub-structures in the north and north-west, where no multiple images were previously known. We identify 75 new multiple images and candidates of 17 sources, 43 of which allow us, for the first time, to constrain the lensing properties and total mass distribution around these extended cluster structures using strong lensing (SL). Our model yields an effective Einstein radius of $\theta_{\rm E,\,main} = 23.2 \pm 2.3$ arcsec for the main cluster core (for $z_{\rm s} = 2$), enclosing a mass of $M(< \theta_{\rm E,\,main}) = (7.7 \pm 1.1) \times 10^{13}\,{\rm M}_{\odot}$, and $\theta_{\rm E,\,NW} = 13.1 \pm 1.3$ arcsec for the newly discovered north-western SL structure enclosing $M(< \theta_{\rm E,\,NW}) = (2.2 \pm 0.3) \times 10^{13}\,{\rm M}_{\odot}$. The northern clump is somewhat less massive with $\theta_{\rm E,\,N} = 7.4 \pm 0.7$ arcsec enclosing $M(< \theta_{\rm E,\,N}) = (0.8 \pm 0.1) \times 10^{13}\,{\rm M}_{\odot}$. We find the northern sub-structures of Abell 2744 to broadly agree with the findings from weak lensing analyses and align with the filamentary structure found by these previous studies. Our model in particular reveals a large area of high magnification values between the various cluster structures, which will be paramount for lensed galaxy studies in the UNCOVER field. The model is made publicly available to accompany the first UNCOVER data release.

Key words: gravitational lensing: strong – galaxies: clusters: individual: Abell 2744 – galaxies: haloes – dark matter – large-scale structure of Universe.

1 INTRODUCTION

Galaxy clusters are the most massive gravitationally bound structures in the Universe. As such, they form relatively late in the hierarchical cosmic history, around $z \lesssim 1$–3 (e.g. Amoura et al. 2021). Clusters form at the nodes of the cosmic web (e.g. Zeldovich, Einasto & Shandarin 1982; de Lapparent, Geller & Huchra 1986) where streams of matter and galaxies fall in towards the dense cluster cores, as shown in detailed *N*-body simulations (e.g. Klypin & Shandarin 1983; Springel et al. 2005; Dubois et al. 2014; Hatfield et al. 2019; Ata et al. 2022). Indeed, massive galaxy clusters often show merging sub-structures in their central regions, along with disturbed X-ray gas or intra-cluster light (ICL) morphologies, whereas some also show prominent cluster structures far outside their core (e.g. Borgani & Guzzo 2001; Ebeling, Barrett & Donovan 2004; Kartaltepe et al. 2008; Jauzac et al. 2012, 2016, 2018; Durret et al. 2016; Medezinski et al. 2016; Ellien et al. 2019; Kim et al. 2019; Asencio, Banik & Kroupa 2021; Diego et al. 2023). The existence, and the observed number of the most massive galaxy clusters can be confronted with expectations from Lambda cold dark matter (ΛCDM) cosmology (e.g. Mullis et al. 2005; Ebeling et al. 2007; Foley et al. 2011; Stanford et al. 2012; Wang et al. 2016; Miller et al. 2018; Asencio et al. 2021) and therefore help constrain the formation and evolution of large-scale structures in the Universe.

One of the most direct methods to detect massive clusters and constrain their total matter distributions is through their gravitational lensing signatures. Although the triaxial shape of clusters creates some bias towards clusters that are elongated along the light of sight (e.g. Hennawi et al. 2007; Okabe, Okura & Futamase 2010; Sereno, Jetzer & Lubini 2010; Oguri et al. 2012), strong lensing (SL) clusters showing a large number of multiply imaged features are often also the most massive galaxy clusters. These are usually either more concentrated, with higher masses in their central core (e.g. Broadhurst & Barkana 2008; Broadhurst et al. 2008), or yet un-virialized merging systems with multiple cores and dark matter (DM) sub-structures enhancing the SL regime (e.g. Meneghetti, Bartelmann & Moscardini 2003; Torri et al. 2004; Meneghetti et al.

★ E-mail: furtak@post.bgu.ac.il

2007a, b; Redlich et al. 2012; Zitrin et al. 2013a). Gravitational lensing, and in particular the SL regime, thus represents a unique means to probe the otherwise invisible DM distribution in massive galaxy clusters.

Galaxy clusters also act as 'cosmic telescopes': The gravitational magnification of background objects allows us to detect and study high-redshift galaxies that would otherwise be too faint to be observed (e.g. Maizy et al. 2010; Kneib & Natarajan 2011; Sharon et al. 2012; Monna et al. 2014; Richard et al. 2014; Zitrin et al. 2014; Coe, Bradley & Zitrin 2015; Coe et al. 2019). Indeed, several observational campaigns targeting galaxy clusters undertaken over the past decade with the *Hubble Space Telescope (HST)*, often complemented by ground-based observations, have led to the detection of several hundreds of lensed high-redshift galaxies at $z > 6$, down to UV luminosities of $M_{\rm UV} \lesssim -13$ (e.g. Bouwens et al. 2017, 2022; Livermore, Finkelstein & Lotz 2017; Atek et al. 2018; Ishigaki et al. 2018) and stellar masses $M_\star \gtrsim 10^6\,{\rm M}_\odot$ (Bhatawdekar et al. 2019; Kikuchihara et al. 2020; Strait et al. 2020, 2021; Furtak et al. 2021). These campaigns to observe SL clusters have also enabled the spectacular detections of transient phenomena such as lensed supernovae (e.g. Kelly et al. 2015, 2016a, b; Rodney et al. 2015, 2021) and even single stars (e.g. Kelly et al. 2018; Welch et al. 2022; Meena et al. 2023a).

Abell 2744 (e.g. Abell, Corwin & Olowin 1989; Allen 1998; Ebeling et al. 2010) at $z_{\rm d} = 0.308$ has by now become a well-studied galaxy cluster. Largely owing to its lensing strength, it was chosen for the *Hubble Frontier Fields* (HFF; Lotz et al. 2017) program, an *HST* Director's Discretionary Time (DDT) program that targeted six lensing clusters to unprecedented depth. Abell 2744 has also been extensively targeted by other ground- and space-based follow-up programs. In terms of SL analyses, the main cluster core was first analysed in Merten et al. (2011) using the `Light-Traces-Mass` modelling method (Zitrin et al. 2009), revealing a large number of multiply imaged systems. Merten et al. (2011) also used X-ray data and performed a wider-field weak lensing (WL) analysis, finding other massive structures around the main clump, which already hinted at the merging history of the cluster. Several lens modelling teams have since published SL models for the core of Abell 2744 based on HFF imaging and spectroscopic follow-up campaigns (Johnson et al. 2014; Richard et al. 2014; Jauzac et al. 2015; Wang et al. 2015; Kawamata et al. 2016, 2018; Priewe et al. 2017). These also yielded numerous lensed high-redshift galaxies behind Abell 2744 (e.g. Atek et al. 2014, 2015; Zheng et al. 2014; Ishigaki et al. 2015), including a triply imaged $z \sim 10$ galaxy (Zitrin et al. 2014), recently confirmed spectroscopically by Roberts-Borsani et al. (2022), and a multiply imaged candidate system at $z \sim 7$–8 (Atek et al. 2014; Mahler et al. 2018), which we confirm is a triply imaged high-redshift object. This particular object seems to be a uniquely red and compact high-redshift object, potentially quasar-like, as presented in detail in a dedicated paper (Furtak et al. 2022). The detailed WL studies in a wide field around the core revealed substantial extended DM sub-structures to the far north and north-west of the cluster core, which seem to hint at a large-scale filamentary structure (Jauzac et al. 2016; Medezinski et al. 2016). The most recent SL models of the cluster were published by Mahler et al. (2018), refined in Richard et al. (2021), and by Bergamini et al. (2023). The Mahler et al. (2018) model is constrained by 188 multiple images, many of which are photometric, and the Bergamini et al. (2023) model includes 90 spectroscopically confirmed multiple images in the main cluster centre. Both of these state-of-the-art models included DM halo components far (∼3 arcmin) outside the main cluster core. These were included to account for the substructures discovered in previous WL analyses, and following galaxy overdensities seen in wider-field *HST* imaging around the cluster. However, due to the lack of ultra-deep high-resolution imaging, and thus SL constraints far from the cluster centre, these external DM haloes were not directly constrained in these models.[1]

This now changes due to the unprecedented sensitivity and spatial resolution of the *JWST* (Gardner et al. 2006; McElwain et al. 2023), the advent of which has already revealed numerous new SL features in several clusters and enabled significant improvements to their SL models (Caminha et al. 2022; Hsiao et al. 2022; Pascale et al. 2022; Diego et al. 2023; Mahler et al. 2023; Meena et al. 2023b; Williams et al. 2023). Most recently, the *JWST* targeted Abell 2744 in the framework of the *Ultra-deep NIRSpec and NIRCam ObserVations before the Epoch of Reionization* (UNCOVER) program (PIs: I. Labbé & R. Bezanson; Bezanson et al. 2022) for wide-field ultra-deep imaging of the cluster and its surroundings (it was also observed to lesser depth in two other *JWST* programs; see Section 2). These new observations now reveal spectacular multiple imaging and strongly lensed arcs also outside the core of Abell 2744, namely around the northern and most prominently the north-western sub-structures. In this work, we use the UNCOVER imaging to identify and classify these new SL constraints and for the first time directly constrain the northern and north-western extensions of the cluster, with a total of 43 new multiple images. These are then incorporated into a new parametric SL model containing the entire central UNCOVER field of view, covering a total area of about 7.6 arcmin × 7.6 arcmin. The lensing maps of our model are made publicly available as part of the UNCOVER data product release.[2]

This paper is organized as follows: We briefly present the targeted cluster and the data used in this analysis in Section 2, before describing our modelling methods and the newly identified lensed features used to constrain our SL model in Section 3. We present and discuss the results in Section 4 and the work is concluded in Section 5. Throughout this paper, we assume a standard flat ΛCDM cosmology with $H_0 = 70\,\frac{\rm km}{\rm s\,Mpc}$, $\Omega_\Lambda = 0.7$, and $\Omega_{\rm m} = 0.3$. All magnitudes quoted are in the AB system (Oke & Gunn 1983) and all quoted uncertainties represent 1σ ranges unless stated otherwise.

2 OBSERVATIONS AND DATA

As one of the six HFF clusters, Abell 2744 (A2744 hereafter) is a well-studied gravitational lensing system and has been targeted by many imaging and spectroscopic campaigns spanning multiple wavelength regimes. Among the ancillary data, the most relevant for this study are of course the HFF *HST* images, which were recently complemented with the *Beyond Ultra-deep Frontier Fields And Legacy Observations* (BUFFALO; PIs: C. Steinhardt & M. Jauzac; Steinhardt et al. 2020) to extend the area of the *HST* coverage around the cluster centre. In addition, there were extensive spectroscopic campaigns of the HFF clusters, both with the *HST* from space in e.g. the *Grism Lens-Amplified Survey from Space* survey (GLASS; Treu et al. 2015) and from the ground with *Keck* and ESO's *Very Large Telescope* (VLT). The former was recently complemented with the

[1] Though see our latest *HST*-based model used in Roberts-Borsani et al. (2022) where we included three tentative multiple systems identified around the two northern clumps in archival *HST* data in a first attempt to constrain these sub-structures.

[2] The maps can be found in the following repository: https://jwst-uncover.github.io/DR1.html##LensingMaps, which is part of the UNCOVER website https://jwst-uncover.github.io.

first *JWST* spectroscopy of A2744 in the framework of the GLASS-*JWST* Early Release Science (ERS) program (Treu et al. 2022) targeted at the cluster core. A2744 is also part of the *ALMA Frontier Fields* survey (González-López et al. 2017) which obtained 1.1 mm imaging of the cluster core with the *Atacama Large Millimeter/submillimeter Array* (ALMA) Band 6 and which will be complemented with additional observations covering the entire UNCOVER footprint (Program ID: 2022.1.00073.S; PI: S. Fujimoto).

In the following text, we concentrate on the data sets that are directly used in this study to construct our SL model of the cluster, i.e. the UNCOVER *JWST* imaging in Section 2.1 and existing *HST* imaging and ground-based spectroscopy in Section 2.2.

2.1 *JWST* UNCOVER imaging

The UNCOVER imaging of A2744 comprises extremely deep observations of the cluster and its surrounding field with the *Near Infrared Camera* (NIRCam; Rieke et al. 2023) aboard the *JWST*, achieving nominal 5σ depths of the order of 29.8 mag before accounting for magnification. The magnification on average adds $\sim$2 mag to the depths in the SL regime, so that UNCOVER effectively reaches down to $\sim$32 mag. The cluster was observed in six broad-band filters, *F*115*W*, *F*150*W*, *F*200*W*, *F*277*W*, *F*356*W*, and *F*444*W*, and in one medium-band filter, *F*410*M*, for 4–6 h each. The data were then reduced and drizzled into mosaics with the `grism redshift and line analysis software for space-based spectroscopy` (`grizli`.[3]; Brammer et al. in preparation). These mosaics also incorporate the other public *JWST* imaging data available in the vicinity of A2744, namely the GLASS-*JWST* (Treu et al. 2022) images obtained with NIRCam and the *Near-Infrared Imager and Slitless Spectrograph* (NIRISS; Doyon et al. 2012, 2023), which in particular add *F*090*W*-band coverage in parts of the UNCOVER field, and the NIRCam imaging obtained in DDT program 2767 (PI: P. Kelly). For this work we use the `v5.4` UNCOVER mosaics, which are publicly available on the UNCOVER website[4] and will also soon be available on the `Barbara A. Mikulski Archive for Space Telescopes (MAST)`. We refer the reader to the UNCOVER survey paper (Bezanson et al. 2022) for more details on the *JWST* data. With a field of view totaling $\sim$45 arcmin^2, the UNCOVER mosaics represent the widest ultra-deep imaging coverage of A2744 to date. Note that deep *Near Infrared Spectrograph* (NIRSpec; Ferruit et al. 2022; Jakobsen et al. 2022; Böker et al. 2023) observations for UNCOVER are scheduled for 2023 July.

In our analysis we furthermore use the first team-internal versions of the UNCOVER photometric catalogues, produced with a python implementation of `SEXTRACTOR` (`SEP`; Bertin & Arnouts 1996; Barbary 2016; Barbary 2018), which will be published in subsequent UNCOVER data releases as detailed in Weaver et al. (2023). These catalogues also contain photometric redshifts measured with `EAZY` (Brammer, van Dokkum & Coppi 2008) and gravitational magnifications derived from the lens model presented in this work.

2.2 Archival *HST* and ground-based data

In addition, the UNCOVER data products encompass *HST* mosaics drizzled to the same pixel-scale and WCS grid as the *JWST* imaging with `grizli`. Therefore, we also incorporate the HFF and extended-area BUFFALO observations in the *Advanced Camera for Surveys* (ACS) *F*435*W*, *F*606*W*, and *F*814*W* filters, and the *Wide-Field Camera Three* (WCF3) *F*105*W*, *F*125*W*, *F*140*W*, and *F*160*W* filters in our analysis.

We use the spectroscopic redshift catalogues constructed by Mahler et al. (2018), refined in Richard et al. (2021), and Bergamini et al. (2023). These were measured using the deep and wide-field observations of A2744 obtained with the *Multi-Unit Spectroscopic Explorer* (MUSE; Bacon et al. 2010) on the VLT in the framework of the MUSE guaranteed time observations (GTO; Program ID: 094.A-0115; PI: J. Richard). The data reduction is described in detail in Richard et al. (2021). Additional redshifts for cluster galaxies used in this work were compiled in Bergamini et al. (2023) using data from GLASS, *VIsible Multi-Object Spectrograph* (VIMOS; Braglia et al. 2009), and *Anglo-Australian Telescope* (AAT; Owers et al. 2011).

3 STRONG LENSING MASS MODELLING

In this section, we present our methods and the constraints used to construct the mass model of A2744. The lens modelling code is explained in Section 3.1. Our SL mass model of A2744 essentially takes two input components from the imaging and spectroscopy data: the cluster member galaxies (Section 3.2) and the lensed multiple image systems (Section 3.3). Finally, we explain our initial set-up of the A2744 SL model in Section 3.4.

3.1 Modelling method

To model A2744 we use a code recently developed for fast parametric lens modelling of galaxy clusters. The method is an updated version of the previous (grid-based) parametric method presented in Zitrin et al. (2013a, b, 2015) and Zitrin (2021), revised to now be completely 'analytic' in the sense that the model is not limited by an input grid resolution. The code was tested on self-simulated mock mass distributions: Using the same mass parametrizations as used for the modelling, a suite of order $\sim$10 arbitrary mass distributions was generated by specifying for each one the input parameter values (namely core and truncation radii, and velocity dispersion of a reference galaxy, and the various DM halo parameters). We then planted sources behind the cluster and lensed them through the simulated mock cluster lens to predict the locations of their multiple images. SL models for these mock clusters were then constructed using these multiple images as input for the minimization, in order to test how well the input parameter values can be recovered. The code was found to work very well, recovering the input parameters to well below the 1σ errors, both using lens and source plane minimizations. First successful models using this method with *JWST* data were published in Pascale et al. (2022) for SMACS J0723.3-7327, where initial details about the modelling method were given, in Hsiao et al. (2022) and Meena et al. (2023b) for MACS J0647.7+7015, and in Williams et al. (2023) for RX J2129.4+0009. An *HST*-based A2744 model with this method was recently also used in Roberts-Borsani et al. (2022). The code is sometimes referred to as '`ZITRIN-ANALYTIC`' in these works.

The method is similar in essence to other, commonly used parametric techniques [e.g. `LENSTOOL` (Kneib et al. 1996; Jullo et al. 2007; Jullo & Kneib 2009), `GLAFIC` (Oguri et al. 2010), `GLEE` (Halkola, Seitz & Pannella 2006; Grillo et al. 2015), etc.], and consists of two main mass components. The first mass component comprises the cluster galaxies, each galaxy modelled as a double Pseudo Isothermal Ellipsoid (dPIE; Elíasdóttir et al. 2007) with projected surface mass

[3] https://github.com/gbrammer/grizli
[4] https://jwst-uncover.github.io/DR1.html

density:

$$\Sigma(\xi) = \frac{\sigma_v^2 r_{\rm cut}^2}{2G(r_{\rm cut}^2 + r_{\rm core}^2)} \left[\left(1 + \frac{r_{\rm core}^2}{\xi^2}\right)^{-\frac{1}{2}} - \left(1 + \frac{r_{\rm cut}^2}{\xi^2}\right)^{-\frac{1}{2}} \right], \quad (1)$$

where σ_v, $r_{\rm core}$, and $r_{\rm cut}$ are the velocity dispersion, core radius, and truncation radius, respectively, and ξ is an elliptical coordinate defined as

$$\xi^2 = \frac{x^2}{(1-\epsilon)^2} + \frac{y^2}{(1+\epsilon)^2}, \quad (2)$$

with ellipticity ϵ. In order to optimize the computation speed, we model most cluster galaxies as spherical ($\epsilon = 0$). The ellipticity is used however for brightest cluster galaxies (BCGs) and equation (1) is in practice implemented as in e.g. Keeton (2001) and Oguri et al. (2010), where it is referred to as a 'Pseudo-Jaffe profile' after Jaffe (1983). The total mass associated with a dPIE profile is then

$$M_{\rm tot} = \frac{\pi \sigma_v^2}{G} \frac{r_{\rm cut}^2}{r_{\rm cut} + r_{\rm core}}. \quad (3)$$

In order to drastically reduce the otherwise large number of free parameters that would arise from modelling each cluster galaxy individually, we use common scaling relations:

$$\sigma_v = \sigma_{v,\star} \left(\frac{L}{L_\star}\right)^{\lambda}, \quad (4)$$

$$r_{\rm core} = r_{{\rm core},\star} \left(\frac{L}{L_\star}\right)^{\beta}, \quad (5)$$

$$r_{\rm cut} = r_{{\rm cut},\star} \left(\frac{L}{L_\star}\right)^{\alpha}, \quad (6)$$

which are based on e.g. the Tully–Fisher (Tully & Fisher 1977) and Faber–Jackson relations (Faber & Jackson 1976) and the fundamental plane to tie the individual dPIE parameters of each galaxy to its luminosity L and scale them with respect to a reference galaxy (e.g. Halkola et al. 2006, 2007; Jullo et al. 2007; Monna et al. 2014, 2015). The three parameters $\sigma_{v,\star}$, $r_{{\rm core},\star}$, and $r_{{\rm cut},\star}$ are those of a reference galaxy of luminosity $L_\star$ and can be left as free parameters in the model. Note that $r_{{\rm core},\star}$ is typically fixed however and only $\sigma_\star$ and $r_{{\rm cut},\star}$ are iterated for. The scaling parameters λ, β, and α can also be left as free parameters in the modelling. For example, Jullo et al. (2007) use $\lambda = 0.25$, $\beta = 0.5$, and $\alpha = 0.5$, for a constant mass-to-light ratio, or $\alpha = 0.8$ to more closely match the fundamental plane. As another example, Monna et al. (2015) for instance do not adopt a core for the galaxies, and have $\lambda = 0.3$ and $\alpha = 0.4$. Note that unless these are specifically left to vary freely, the scaling relations (4)–(6) are also applied to the BCGs.

The second mass component consists of the diffuse cluster DM haloes. These are modelled as Pseudo Isothermal Elliptical Mass Distributions (PIEMDs; e.g. Jaffe 1983; Keeton 2001)

$$\Sigma(\xi) = \frac{\sigma_v^2}{2G} \left(r_{\rm core}^2 + \xi^2\right)^{-\frac{1}{2}}. \quad (7)$$

One such diffuse cluster halo is usually sufficient for a relaxed cluster with a single prominent BCG, but several cluster haloes are often needed to model merging or complex clusters, i.e. those containing various sub-structures and BCGs such as A2744 (e.g. Jauzac et al. 2015; Mahler et al. 2018; Bergamini et al. 2023).

In addition, a two-component external shear can be applied, which can sometimes help account for external contributions not taken into account in the mass modelling. Source redshifts can be left as free parameters, especially for galaxies lacking spectroscopic redshifts, and the weight of individual cluster galaxies can also be left to be freely optimized. The latter can be applied in two ways – either by incorporating the relative weight factor directly to the luminosity of the galaxy, affecting correspondingly all quantities derived from the scaling relations (this is the default choice), or if desired, only to the velocity dispersion of the galaxy, without affecting its other parameters. Similarly, the ellipticity parameters and core radii of the BCGs can also be left to be freely optimized. Finally, the code also allows for the incorporation of time delays, magnification ratios, and image parity information.

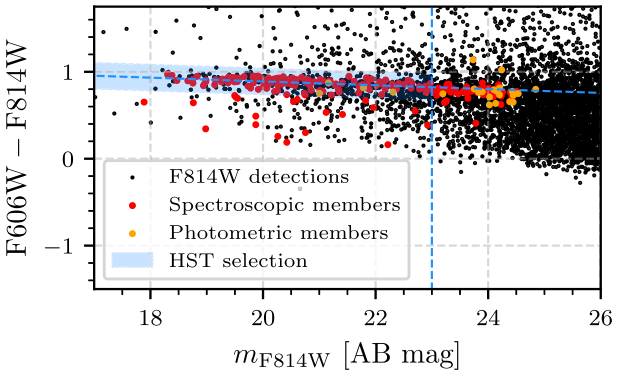

Figure 1. *HST* colour–magnitude diagram of objects detected in A2744, showing the cluster's red sequence. The known cluster members from Bergamini et al. (2023) are shown in red and orange dots, and our red sequence selection is shown as the blue shaded area.

3.2 Cluster member galaxies

We compile the list of cluster member galaxies hierarchically using all of the available data sets in the following way: We first include the 225 cluster members used in Bergamini et al. (2023), 202 of which are spectroscopically confirmed to lie at the cluster redshift, $z_{\rm d} = 0.308$. These were mostly derived from MUSE observations, as well as other ancillary catalogues listed in Section 2.2. This spectroscopic sample is then used to calibrate red-sequence selection criteria aimed at identifying cluster member galaxies that lie beyond the MUSE coverage.

At the cluster redshift, the 4000 Å-break falls between the *HST*/ACS *F*606*W* and *F*814*W* bands. Because of that, these two filters are optimal for identifying the red sequence of A2744. We therefore perform a cluster member selection using the *HST* data (see Section 2.2) which are much more extended than the initial HFF footprint owing to the wide-field BUFFALO and parallel field data. Galaxies are detected with SEXTRACTOR (Bertin & Arnouts 1996) in the *F*814*W*-band and photometry is measured in both ACS bands. The thus obtained colour–magnitude diagram clearly shows the cluster's red sequence, as can be seen in Fig. 1. We fit a linear relation to the *F*606*W*–*F*814*W* colour of the Bergamini et al. (2023) spectroscopic cluster members and use the result to select *HST*-detected galaxies in a colour window of width 0.3 mag around that relation with magnitudes $m_{F814W} \leq 23$ mag as cluster members. Note that this magnitude cut is only applied to the colour-selected galaxies; we include all spectroscopically confirmed cluster members regardless of their brightness.

With this selection, we end up with a cluster member catalogue containing 421 galaxies. Most notable are of course the two well-known BCGs, BCG1 and BCG2, in the cluster core. In addition, the cluster has two BCGs at the position of the north-western extension, which we will denote NW-BCG1 and NW-BCG2, and one in the northern sub-structure which we will denote N-BCG. While these sub-structures were included as fixed or free DM clumps in previous

SL models of A2744 (Mahler et al. 2018; Bergamini et al. 2023), we are able to confirm them as SL structures for the first time due to the UNCOVER imaging and constrain their parameters as will be shown in more detail in Sections 3.3 and 4. The wide *HST* coverage of the UNCOVER field reveals cluster member galaxies out to 4.11 arcmin from BCG1, which corresponds to 1.12 Mpc at the cluster redshift. Together with the *JWST* UNCOVER data revealing a trove of SL constraints (see Section 3.3), these now confirm the extended merging nature of A2744 already indicated by the previous X-ray and WL analyses (Merten et al. 2011; Jauzac et al. 2016; Medezinski et al. 2016). Note that we will further discuss the large-scale structure of A2744 in light of our SL analysis results in Section 4. The full catalogue of cluster galaxies is included in the public release of our SL model of A2744 (see Section 4).

3.3 Multiple image systems

The SL features at the centre of A2744 have been extensively studied with the exceptionally deep HFF imaging and GLASS and MUSE spectroscopy (see Section 2.2). These data yielded a total of 60 multiply imaged galaxies in A2744, producing 188 images in the cluster core (Mahler et al. 2018; Richard et al. 2021). This list was then recently refined to a secure, purely spectroscopic, sample by Bergamini et al. (2023). For our SL model, we use this secure spectroscopic sample of 90 multiple images belonging to 30 sources to constrain the main cluster core and refer the reader to Bergamini et al. (2023) (table A.1) for a complete list of images and redshifts. To this we add the triply imaged Zitrin et al. (2014) $z \sim 10$ object which was recently confirmed with *JWST*/NIRSpec spectroscopy at $z_{\rm spec} \simeq 9.76$ (Roberts-Borsani et al. 2022). We also identify a notable triply imaged dropout system at $z \sim 7$–8. Two of its images were previously reported in HFF high-redshift samples (Atek et al. 2014, 2015) and identified as a photometric multiple image system in Mahler et al. (2018), system 53. The new UNCOVER data now not only reveal a third image to this system but together with the SL model also help us further to confirm its high-redshift nature. Furthermore, in the *JWST* observations the object appears to be extremely red and compact with a point-like morphology, suggesting it is potentially an obscured active galactic nucleus (Furtak et al. 2022). Note that this new image was identified after constructing the current lens model and will therefore only be included in future versions released in future UNCOVER data releases.

The new ultra-deep UNCOVER imaging of A2744 reveals spectacular new strongly lensed multiple image systems in the northern and north-western extensions of the cluster. While these extended sub-structures are known from X-ray and WL analyses (Merten et al. 2011; Jauzac et al. 2016; Medezinski et al. 2016), they have so far not yet been confirmed to be dense enough to produce clear SL multiple images. Using the UNCOVER mosaics (see Section 2.1), we identify 17 new multiple image systems and candidate systems in the north-western and one in the northern sub-structure of the cluster in a by-eye search considering their colour, visual aspect, relative geometric position, and parity. The new systems are listed and summarized in Table 1 and can be seen in Figs 2 and 3 for the north-western and northern sub-structures. For systems that lack clear point-like features, we identify locations which show other unique features repeating in all counter images, such as places where the arc gets thicker or thinner, and use these as approximate image positions. The northern sub-cluster has only one clearly identified multiple image system, system 78. Note that we continue from the numbering scheme of Mahler et al. (2018), which was also perpetuated in Bergamini et al. (2023), i.e. we start at 65. Some of these multiple image systems, in particular systems 65, 71, and 78, present several sub-clumps in the *JWST* imaging, each of which can be used as an independent source in the SL modelling. Taking these into account, we identify a total of 75 new multiple images and image candidates in the north-western and northern sub-structures of A2744. Note that we do not use candidate multiple images, marked 'c' in Table 1, in the lens model (see Section 3.4).

Some of these new multiply imaged galaxies are of particular interest for other studies. For example, the four relatively bright red systems 66 to 69 and the fainter candidate system c79 (see Fig. 2) are completely invisible in the *HST* data but all have well-constrained photometric redshifts in the preliminary UNCOVER stellar population analysis (see Section 2.1) $z_{\rm phot} \simeq 2.2$–2.5. This hints as to their probably very dusty nature and their apparent spatial proximity could indicate an overdensity at $z \sim 2.5$. Indeed, the *JWST* has already revealed a population of such red galaxies around the cosmic noon and even up to the epoch of cosmic reionization (e.g. Fudamoto, Inoue & Sugahara 2022; Naidu et al. 2022; Barrufet et al. 2023; Glazebrook et al. 2023; Nelson et al. 2023; Nonino et al. 2023; Zavala et al. 2023), similarly to these galaxies. Systems 68 and 69 each show a relatively bright radial image close to the north-western BCG2, as can also be seen in Fig. 2, which are of particular value to constrain the mass distribution of that cluster galaxy. We have furthermore tentatively identified a candidate multiply imaged high-redshift source, system c80, which shows various multiply imaged clumps. These images show flux in the UNCOVER bands, i.e. in *F*115*W* and red-ward, but are invisible in the *HST* filters which could mean that they are *F*814*W*-dropouts at $z \sim 7$–8. This is also supported by our lens model (see the high-redshift critical curve in Fig. 2) presented in Section 4. Note however that the BUFFALO coverage in this part of the cluster is much shallower than the central HFF observations such that a low-redshift solution cannot be ruled out at this stage. We will therefore need spectroscopic observations of this object with *JWST*/NIRSpec to accurately determine its redshift and perhaps multiply imaged nature.

3.4 Model set-up

Since A2744 is known to be a complex merging cluster, we follow the previously published SL models (e.g. Jauzac et al. 2015; Mahler et al. 2018; Bergamini et al. 2023) and place two PIEMD DM haloes in the cluster core, initially centred on the two BCGs but with a free centre position that is none the less limited to the vicinity ($\lesssim$3 arcsec) of the BCGs. In addition, we leave the weights of the two BCGs free as well as those of several other galaxies situated close to multiple images (see Fig. 4). For BCG1 (see Section 3.2) we also leave the ellipticity parameters free but fix them to the SEXTRACTOR-measured values for BCG2.

In order to model the newly discovered SL structures in the north-west and in the north (see Sections 3.2 and 3.3), we place two PIEMD haloes in the north-western sub-structure, centred on the two BCGs, and another one fixed on the northern BCG. The centres of the two north-western haloes are left free within 3 arcsec of their respective BCG. We also allow for the ellipticity parameters, weight, and the core radius of the NW-BCG2 to vary since they lie very close to the radial images of systems 68 and 69. A cluster galaxy next to images 68.2 and 69.2 is also left with a free weight (see Fig. 2). Finally, we fix the value of the reference galaxy core radius in equation (5) to $r_{\rm core,\star} = 0.2$ kpc, similar to other SL works (e.g. Richard et al. 2014). Such values, namely $r_{\rm core,\star} =$

0.2 kpc, are typical of elliptical galaxies (e.g. Wallington & Narayan 1993).

Our SL model is constrained with a total of 135 multiple images, 92 of which have spectroscopic redshifts and are situated in the cluster core as detailed in Section 3.3. Among the remaining images, 37 lie in the north-western extension and six in the northern sub-structure. For all systems with available spectroscopic redshifts, the redshift is fixed to the measured one in the model. In addition, as can be seen in Table 1, systems 66 to 69 and system 72 have relatively well-constrained photometric redshifts. We therefore leave these redshifts as free parameters in the model but limit them to the 97.5 per cent ranges of their photometric redshifts, which are relatively narrow ($\Delta z \lesssim 0.4$). All other source redshifts are left free to vary between $z_s = 0.8$ and $z_s = 10$. Note that no parity information is used in this model.

The model is optimized using a Monte Carlo Markov Chain (MCMC) analysis in two steps: First by running ∼150 relatively short chains of several thousand steps each to explore the parameter space, derive the covariance matrix encoding the correlations between the different parameters, and potentially to approach the global minimum

Table 1. New multiple images and candidates identified in the northern and north-western extensions of A2744.

ID	RA	Dec.	z_{phot} [97.5 per cent range]	z_{model} [95 per cent range]	Remarks
65.11	00:14:13.570	−30:22:32.649	–	2.798 [2.473,3.106]	Close to north-western BCG1.
65.12	00:14:13.521	−30:22:36.422	–	”	”
c65.13	00:14:13.105	−30:22:45.219	3.483 [3.258,3.741]	’	Candidate counter image.
c65.13	00:14:12.979	−30:22:47.563	–	”	”
65.21	00:14:13.571	−30:22:32.916	–	”	Close to north-western BCG1.
65.22	00:14:13.530	−30:22:36.165	–	”	”
c65.23	00:14:13.084	−30:22:45.594	–	”	Candidate counter image.
c65.23	00:14:12.953	−30:22:47.671	–	”	”
65.31	00:14:13.563	−30:22:34.178	–	”	Close to north-western BCG1.
65.32	00:14:13.556	−30:22:35.004	–	”	”
66.1	00:14:13.113	−30:22:25.817	2.227 [1.994,2.421]	2.413 [2.406,2.420]	
66.2	00:14:12.764	−30:22:33.592	–	”	Close to north-western BCG1.
66.3	00:14:12.556	−30:22:43.000	–	”	
67.1	00:14:10.089	−30:22:28.583	2.423 [2.288,2.510]	2.617 [2.613,2.620]	Bright system, invisible in *HST* data,
67.2	00:14:10.279	−30:22:24.600	2.536 [2.491,2.695]	”	
67.3	00:14:10.632	−30:22:05.019	2.443 [2.347,2.600]	”	
68.1	00:14:09.707	−30:22:30.242	2.524 [2.495,2.698]	2.327 [2.321,2.332]	Bright system, invisible in *HST* data.
68.2	00:14:09.681	−30:22:20.969	–	”	Close to north-western BCG2.
68.3	00:14:10.334	−30:22:05.143	2.443 [2.234,2.621]	”	
68.4	00:14:10.100	−30:22:21.444	–	”	Radial image; close to north-western BCG2.
69.1	00:14:09.773	−30:22:33.161	2.423 [2.228,2.630]	2.432 [2.428,2.436]	Bright system, invisible in *HST* data.
69.2	00:14:09.823	−30:22:19.990	–	”	Close to north-western BCG2.
69.3	00:14:10.344	−30:22:08.778	2.325 [2.224,2.351]	”	
69.4	00:14:10.233	−30:22:20.856	–	”	Radial image; close to north-western BCG2.
70.1	00:14:12.579	−30:22:26.363	–	2.716 [2.500,3.645]	
70.2	00:14:12.565	−30:22:26.675	–	”	
c70.3	00:14:12.109	−30:22:42.648	–	”	
71.11	00:14:13.764	−30:22:41.450	–	1.379 [1.245,1.533]	
71.12	00:14:13.788	−30:22:40.884	–	”	
71.13	00:14:13.819	−30:22:39.388	–	”	
71.21	00:14:13.759	−30:22:41.574	–	”	
71.22	00:14:13.797	−30:22:40.744	–	”	
71.23	00:14:13.819	−30:22:39.597	–	”	
72.1	00:14:11.915	−30:22:42.461	3.657 [3.131,4.088]	3.544 [3.531,3.565]	
72.2	00:14:12.268	−30:22:29.121	–	”	
72.3	00:14:12.552	−30:22:20.067	3.664 [3.234,4.086]	”	
c73.1	00:14:11.508	−30:22:11.886	0.225 [0.042,6.799]	–	
c73.2	00:14:11.252	−30:22:23.351	4.037 [1.173,5.340]	–	
c73.3	00:14:10.810	−30:22:37.163	–	–	
74.1	00:14:10.833	−30:22:29.697	2.707 [1.324,4.563]	3.033 [2.832,3.255]	
74.2	00:14:10.861	−30:22:28.911	4.451 [1.913,4.921]	”	
74.3	00:14:11.289	−30:22:10.152	2.228 [1.834,2.523]	”	
c75.1	00:14:11.525	−30:22:10.488	2.040 [0.409,11.036]	–	
c75.2	00:14:11.174	−30:22:25.668	5.062 [1.103,16.824]	–	
c75.3	00:14:10.850	−30:22:35.548	–	–	
c76.1	00:14:10.746	−30:22:34.898	–	–	
c76.2	00:14:11.046	−30:22:25.827	0.798 [0.113,1.915]	–	
c76.3	00:14:11.396	−30:22:08.988	–	–	

Note. Column 1: Image ID; *Columns 2 and 3*: Right ascension and declination (J2000.0); *Column 4*: Photometric redshift and its 97.5 per cent range taken from the UNCOVER catalogue (see Section 2.1); *Column 5*: Median redshift from our SL-model (see Section 4); *Column 6*: Additional remarks. Candidate images are marked with ‘*c*’ and are not used in the modelling.

Table 1. – *continued*. New multiple images and candidates identified in the northern and north-western extensions of A2744. We also include here two systems lensed by the main cluster core: the $z \simeq 9.8$ system from Zitrin et al. (2014) and Roberts-Borsani et al. (2022), and one dropout $z \sim 7$–8 system (i.e. system 53 Atek et al. 2014; Mahler et al. 2018), which we further confirm with the UNCOVER data. Note that system 53 is not included in the lens modelling at this stage.

ID	RA	Dec.	$z_{\rm phot}$ [97.5 per cent range]	$z_{\rm model}$ [95 per cent range]	Remarks
77.11	00:14:12.439	−30:22:39.334	–	1.505 [1.441,1.582]	
77.12	00:14:12.535	−30:22:35.316	–	,,	
77.13	00:14:12.954	−30:22:22.743	–	,,	
c77.21	00:14:12.493	−30:22:37.781	–	,,	
c77.22	00:14:12.516	−30:22:36.783	–	,,	
c77.31	00:14:12.501	−30:22:37.430	–	,,	
c77.32	00:14:12.511	−30:22:37.016	–	,,	
78.11	00:14:19.108	−30:21:27.791	–	2.571 [2.049,2.767]	Close to northern BCG.
78.12	00:14:19.017	−30:21:28.108	–	,,	,,
78.13	00:14:17.971	−30:21:21.851	–	,,	
78.21	00:14:19.130	−30:21:27.791	–	,,	Close to northern BCG.
78.22	00:14:19.000	−30:21:28.209	–	,,	System redshift poorly constrained.
78.23	00:14:17.980	−30:21:21.877	–	,,	
c79.1	00:14:09.818	−30:22:27.889	2.606 [2.223,2.963]	–	
c79.2	00:14:09.772	−30:22:22.089	–	–	Close to north-western BCG2.
c79.3	00:14:10.429	−30:22:03.847	–	–	
c80.11	00:14:11.153	−30:22:35.005	–	–	Candidate high-redshift object; possible *F*814*W*-dropout.
c80.12	00:14:11.213	−30:22:32.917	–	–	,,
c80.13	00:14:11.286	−30:22:31.056	–	–	,,
c80.14	00:14:11.793	−30:22:10.935	0.706 [0.541,13.853]	–	,,
c80.21	00:14:11.133	−30:22:35.298	11.839 [0.993,15.925]	–	,,
c80.22	00:14:11.195	−30:22:33.287	–	–	,,
c80.23	00:14:11.305	−30:22:30.000	15.104 [1.056,19.585]	–	,,
c80.24	00:14:11.776	−30:22:11.062	12.357 [0.537,14.560]	–	,,
c81.1	00:14:10.713	−30:22:35.817	–	–	
c81.2	00:14:11.104	−30:22:23.761	–	–	
c81.3	00:14:11.367	−30:22:10.528	–	–	
53.1	00:14:19.161	−30:24:05.664	7.188 [7.142,7.165]	–	Detected in HFF (Atek et al. 2014; Mahler et al. 2018).
53.2	00:14:20.051	−30:23:48.058	0.193 [0.189,0.196]	–	‘; heavily affected by the ICL.
53.3	00:14:23.331	−30:23:39.639	7.188 [7.131,8.578]	–	Newly identified in the UNCOVER imaging (Furtak et al. 2022).
JD1A	00:14:22.202	−30:24:05.364	$z_{\rm spec} = 9.76$	–	see Zitrin et al. (2014); Roberts-Borsani et al. (2022)
JD1B	00:14:22.805	−30:24:02.700	‘	–	‘
cJD1C	00:14:18.607	−30:24:31.356	‘	–	

Note. Column 1: Image ID; *Columns 2 and 3*: Right ascension and declination (J2000.0); *Column 4*: Photometric redshift and its 97.5 per cent range taken from the UNCOVER catalogue (see Section 2.1); *Column 5*: Median redshift from our SL-model (see Section 4); *Column 6*: Additional remarks. Candidate images are marked with ‘*c*’ and are not used in the modelling.

of the source plane χ^2-function defined as

$$\chi^2 = \sum_i \frac{(\vec{\beta}_i - \vec{\beta}_0)^2}{\mu_i^2 \sigma_i^2} + \sigma_p p, \tag{8}$$

where $\vec{\beta}_i$ represents the source position of each multiple image, $\vec{\beta}_0$ the common modelled barycentre source position of the images belonging to the same system, and μ_i and σ_i the magnification and positional uncertainty of each multiple image. The second term represents the forced parities where p is the number of images modelled with the wrong parity and σ_p a constant factor to add to the χ^2 for each wrong parity. Note that we perform the minimization in the source plane which in principle should perform just as well as a lens plane minimization (Keeton 2010), as is also evident by the quality of some HFF SL models that were built using a source plane minimization, but has the advantage of being significantly faster. The result from this multichain first step is then further refined with two or more long MCMC chains, each of several $\sim 10^4$ steps and a decreasing ‘temperature’, enabling in practice some annealing. We assume a positional uncertainty of $\sigma_i = 0.5$ arcsec for all multiple images used as constraints. We can also evaluate the χ^2 in the lens plane, defined as

$$\chi^2 = \sum_i \frac{(\vec{\theta}_i - \vec{\theta}_{i,\rm model})^2}{\sigma_i^2} + \sigma_p p, \tag{9}$$

where $\vec{\theta}_i$ is the observed position of the i-th image and $\vec{\theta}_{i,\rm model}$ its predicted position, which should be roughly similar to the source-plane χ^2 (Keeton 2010).

Note that although the nominal positional uncertainty adopted for the multiple images in the χ^2 calculations in (8) and (9) is taken as 0.5 arcsec, the statistical uncertainties of the resulting model parameters are calculated from an MCMC chain that is run with effectively $\sim$3.5 $\times$ that value, 1.76 arcsec. In practice, this is done by adopting a higher temperature when estimating the parameter uncertainties than the nominal one used in the minimization of the final chain, which we have found to be representative of the true parameter uncertainties. Note that this only affects the uncertainty estimate of the parameters and not the best-fitting value or the χ^2 minimization. This factor was estimated previously on mock clusters by repeating the minimization 50 times while perturbing all multiple image positions with a Gaussian of width $\sigma = 0.5$ arcsec in both

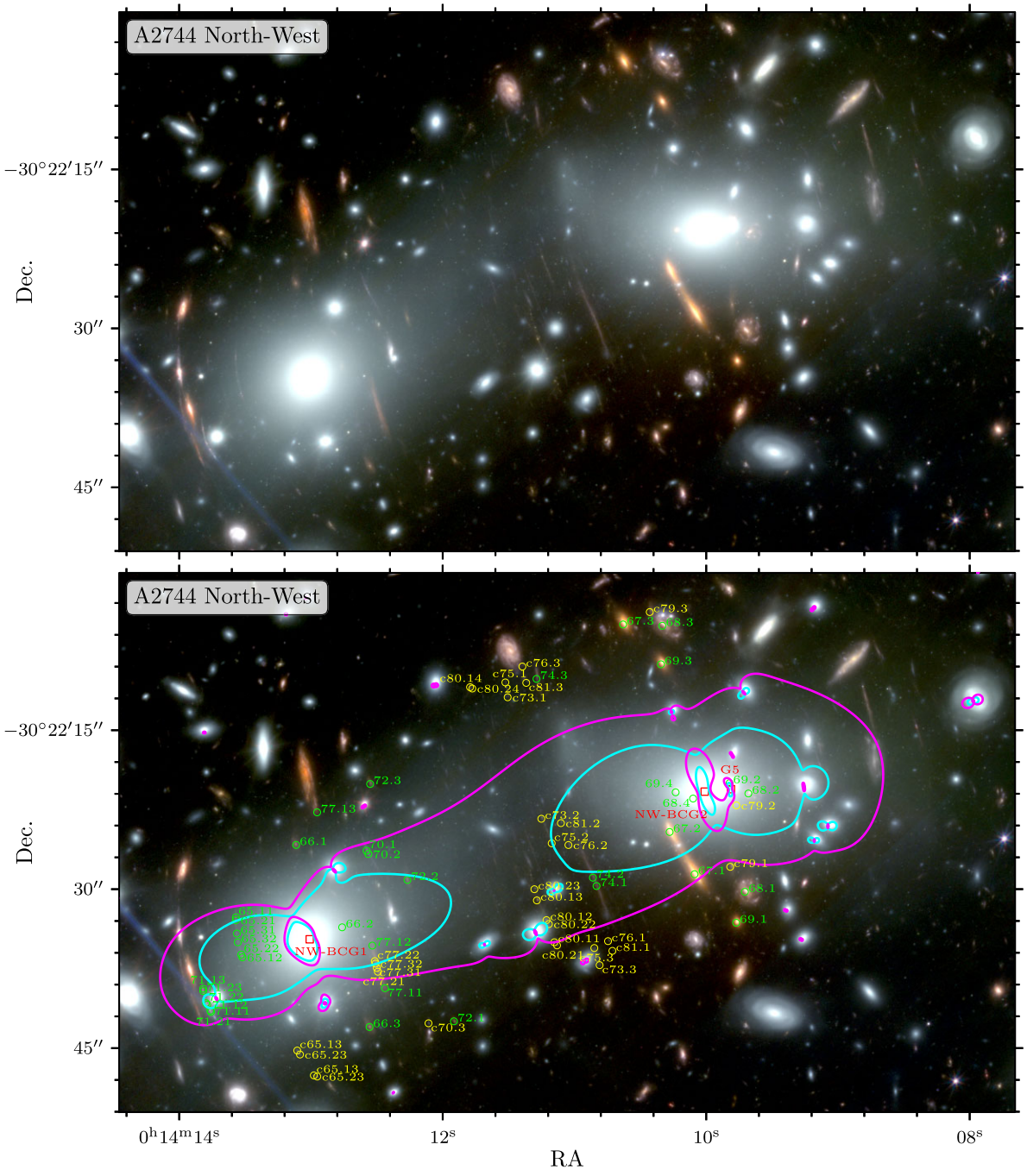

Figure 2. A 1.46 arcmin × 0.85 arcmin cut-out of an UNCOVER colour-composite image exhibiting the many newly discovered SL features and candidates in the north-western sub-structure of A2744. The filter stacks used are: Blue – *F*090*W*+*F*115*W*+*F*150*W*, Green – *F*200*W*+*F*277*W*, and Red – *F*356*W*+*F*410*M*+*F*444*W*. In the bottom panel, we mark the newly identified and numbered multiple image systems in green and multiple image candidates in yellow. These are listed in Table 1. Cluster galaxies left free to vary in our SL model (see Table 3) are shown in red. The critical curves of our SL model (see Section 4) for source redshifts $z_s = 1.6881$, the redshift of system 1 (Mahler et al. 2018), and $z_s = 10$ are shown in blue and purple, respectively.

coordinates in order to assess how the multiple images' positional uncertainty affects the parameter posterior distribution.

4 RESULTS AND DISCUSSION

Our resulting SL model of A2744 has a final *lens plane* χ^2(9) of $\chi^2 = 234$ and an average, lens-plane image reproduction RMS of 0.66 arcsec. Our model has 161 SL constraints (i.e. 2 × 135, the number of images, minus 2 × 46, the number of systems used in the modelling, minus 15, the number of systems whose redshift was left free, after equation 1 in Kneib et al. 1993), and 61 free parameters, which results in 102 degrees of freedom. This nominally leads to a reduced lens plane χ^2 of $\simeq 2.3$, i.e. somewhat above but of order unity. For comparison, our image reproduction RMS is of the same order as quoted for the Mahler et al. (2018) model (0.67 arcsec) and 1.8× higher than the value quoted for the Bergamini et al. (2023) model

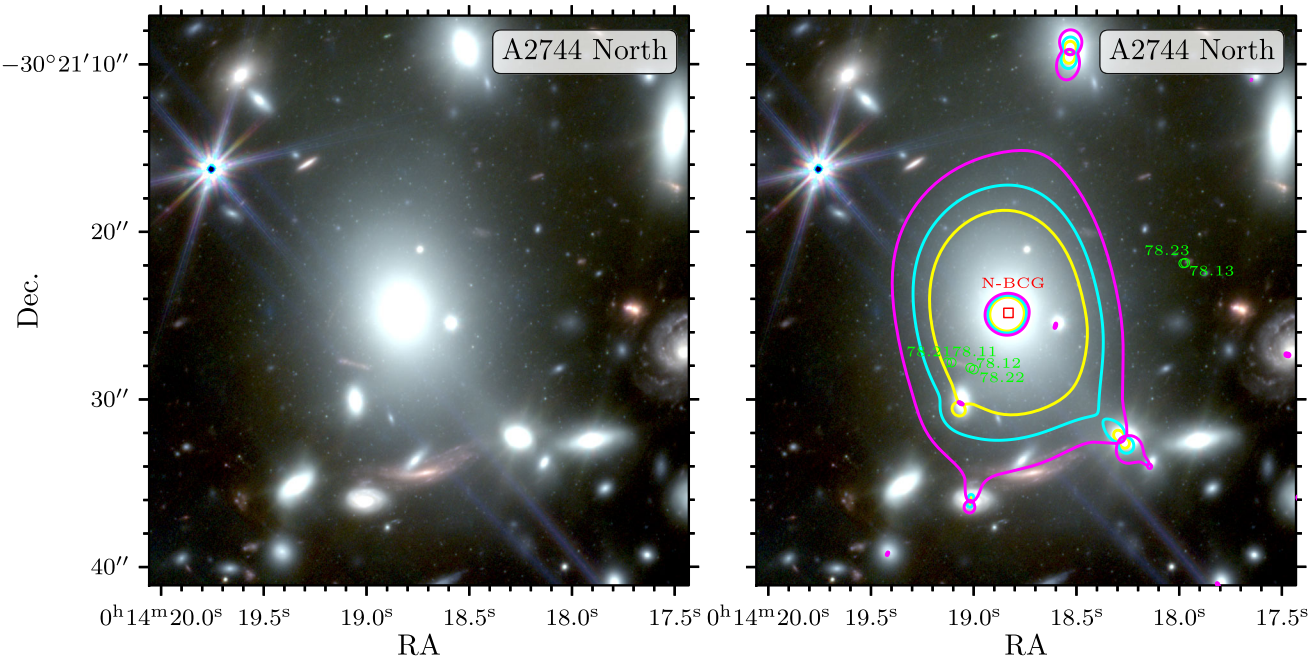

Figure 3. A 34 × 34 arcsec cut-out of an UNCOVER colour-composite image in the same filter configuration as in Fig. 2. In the right-hand panel, we mark the newly identified SL features around the northern sub-structure of A2744. The northern BCG, which is left free to vary in our SL model, is shown in red. We also show the critical curves of our SL model (see Section 4) for source redshifts $z_s = 1$ in yellow, $z_s = 1.6881$ (see Fig. 2) in blue, and $z_s = 10$ in purple. The critical curves from the current model do not pass where we would expect for system 78, suggesting that the system either lies at a lower redshift ($z_s < 1$), that it consists only of two images, or most probably, that the mass of this sub-halo is somewhat overestimated (see discussion in Section 4). A red spiral galaxy south of the N-BCG is notably lensed, i.e. magnified and distorted, but is likely not multiply imaged.

(0.37 arcsec). Note however that we include a multitude (15) of new multiple image systems without precise redshift measurements to constrain the outer sub-structures, as opposed to their secure purely spectroscopic sample in the cluster core. Indeed, e.g. Johnson & Sharon (2016) found that the RMS-scatter in the lens plane may degrade when less spectroscopic systems are used for the modelling. Moreover, caution should be taken when comparing RMS values, which may be calculated somewhat differently in different works or between different modellers.

We show the critical curves for sources at redshifts $z_s = 1.6881$ and $z_s = 10$ in Fig. 4. The redshift $z_s = 1.6881$ corresponds to the redshift of system 1 (Mahler et al. 2018) and represents the redshift to which the distance ratios are normalized in our model. More detailed zoomed-in versions on the extended sub-structures in the north-west and in the north can be seen in Figs 2 and 3, respectively. The figure illustrates how the inclusion of the northern and north-western extensions increases the total critical area of A2744 by a factor ∼1.5. We indeed find a total critical area of $A_{\rm crit} = 0.67\,{\rm arcmin}^2$ which translates into an effective Einstein radius of $\theta_{\rm E} = 27.7 \pm 2.8$ arcsec for a source at $z_s = 2$. The total cluster mass enclosed by those curves is $M(<\theta_E) = (1.07 \pm 0.15) \times 10^{14}\,{\rm M}_\odot$. In particular the area between the main cluster and north-western extension forms a high-magnification 'bridge' where the magnification remains $\mu \gtrsim 4$ for sources at $z_s = 10$ as can be seen in Fig. 5. Individually, the main cluster has a $z_s = 2$ critical area of $A_{\rm crit,main} = 0.47\,{\rm arcmin}^2$ ($\theta_{\rm E,\,main} = 23.2 \pm 2.3$ arcsec) comprising a mass of $M(<\theta_{E,{\rm main}}) = (7.7 \pm 1.1) \times 10^{13}\,{\rm M}_\odot$. The northern and north-western substructures each have critical areas of $A_{\rm crit,N} = 0.05\,{\rm arcmin}^2$ ($\theta_{\rm E,\,N} = 7.4 \pm 0.7$ arcsec) and $A_{\rm crit,NW} = 0.15\,{\rm arcmin}^2$ ($\theta_{\rm E,\,NW} = 13.1 \pm 1.3$ arcsec), enclosing masses of $M(<\theta_{E,{\rm N}}) = (0.8 \pm 0.1) \times 10^{13}\,{\rm M}_\odot$ and $M(<\theta_{E,{\rm NW}}) = (2.2 \pm 0.3) \times 10^{13}\,{\rm M}_\odot$ respectively. Above, we adopt nominal errors of 10 per cent and 14 per cent for the effective Einstein radii and enclosed masses, respectively, which encompass the typical systematic scatter of these values between different models (e.g. Zitrin et al. 2015). The statistical errors that we obtain from our model are smaller, of the order ∼2–3 per cent for the effective Einstein radius and ∼5 per cent for the enclosed total mass.

The median PIEMD parameters of the five DM haloes in our model are listed in Table 2. Note that the northern halo seems to be unexpectedly massive given the apparent dearth of multiple image systems in that region (see Section 3.3). This particular sub-structure is therefore probably poorly constrained due to its lack of many multiple images and spectroscopic redshifts to anchor the model in that region. Because of that, we surmise that this halo in particular might be overestimated in our model. Our results in the main cluster agree well with Mahler et al. (2018) and Bergamini et al. (2023) which is unsurprising since we use a similar set-up and rely on the same set of multiple images and spectroscopic redshifts to constrain this region of the cluster. In particular, the Mahler et al. (2018) model, which achieved a similar lens plane RMS as ours (see above), finds an effective Einstein radius of $\simeq 23.9$ arcsec for $z_s = 4$ (given in Richard et al. 2021) in the main cluster core where our model yields $\theta_{\rm E,\,main} = 26.2 \pm 2.6$ arcsec for the same source redshift. These two models therefore concur within the uncertainties. We also refer the reader to fig. 1 in Roberts-Borsani et al. (2022) where we overlaid the $z_s = 10$ critical curves of our preliminary main cluster core model alongside those of the Zitrin et al. (2014) and Bergamini et al. (2023) models. Furthermore, we find a total cluster mass of $M(r < 200\,{\rm kpc}) = (1.60 \pm 0.22) \times 10^{14}\,{\rm M}_\odot$ within 200 kpc of BCG2 (see Fig. 4) which also agrees with the value found in

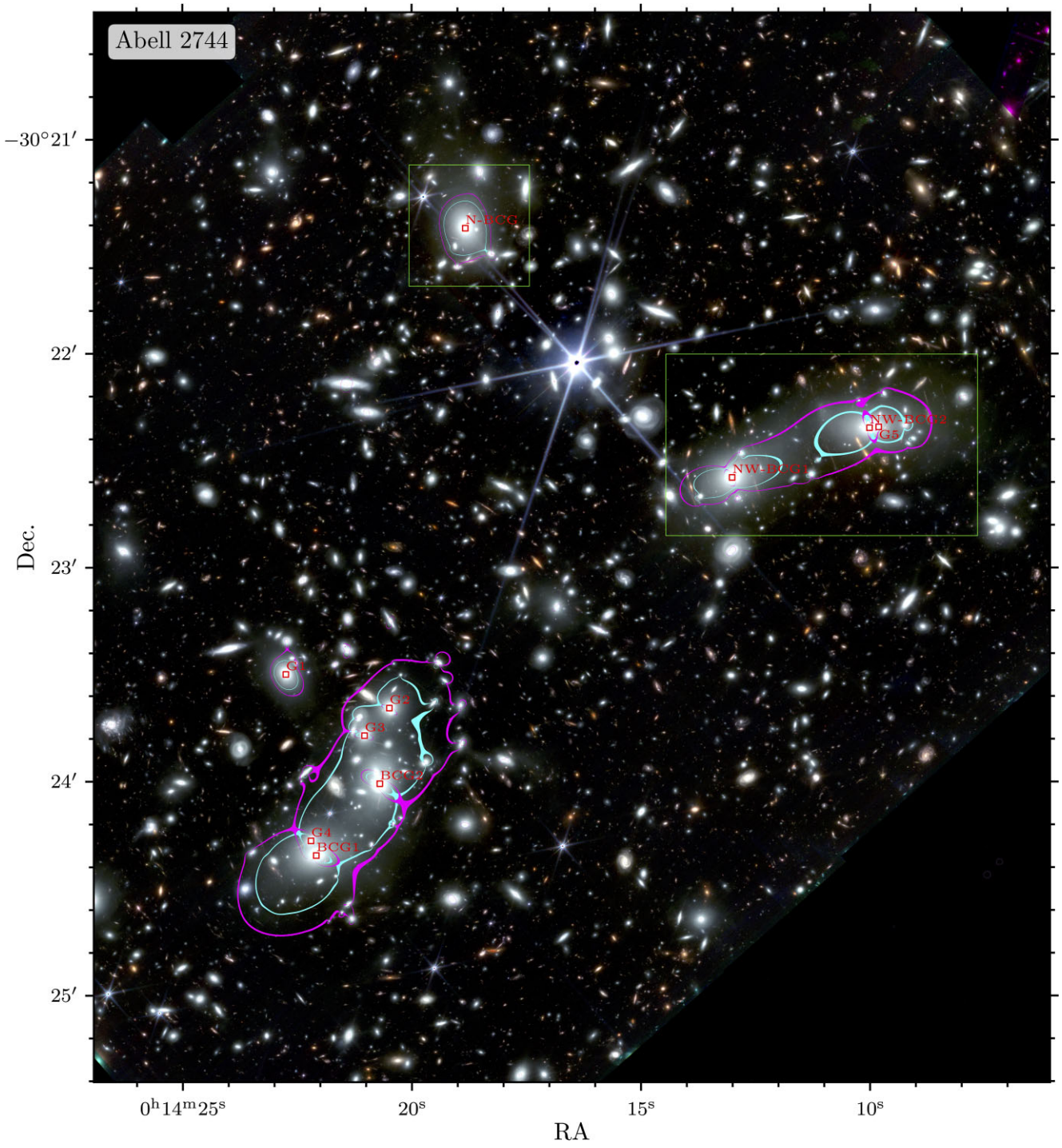

Figure 4. A 4.5 arcmin × 5.0 arcmin cut-out of an UNCOVER/NIRCam composite-colour image of A2744 in the same filter configuration as in Figs 2 and 3. Cluster galaxies left free to vary in our SL model (see Section 3.4 and Table 3) are shown in red. Overlaid we show the critical curves of our SL model for source redshifts $z_s = 1.6881$ (corresponding to system 1) and $z_s = 10$ in blue and purple, respectively, as in Fig. 2. The area between the main cluster and the north-western sub-structure in particular has high magnifications of order $\mu \gtrsim 4$ for sources at $z_s = 10$ (see Fig. 5). The green rectangles outline the fields shown in more detail in Figs 2 and 3. Note, a vectorized full UNCOVER resolution (0.04 arcsec pix^{-1}) version of this figure is available in the online supplemental material of this paper.

Bergamini et al. (2023) within the uncertainties. The two models by Mahler et al. (2018) and Bergamini et al. (2023) also include the extended sub-structures in the north and the north-west based on the previous predictions from WL and the BUFFALO *HST* imaging, but do not constrain them directly due to the lack on SL features in that region prior to the UNCOVER imaging. With the new multiple images identified in this study, however, we find much less massive DM haloes than Mahler et al. (2018) and slightly less massive haloes than Bergamini et al. (2023) in these structures. In particular, the northern DM halo has a much lower mass in our model (see Table

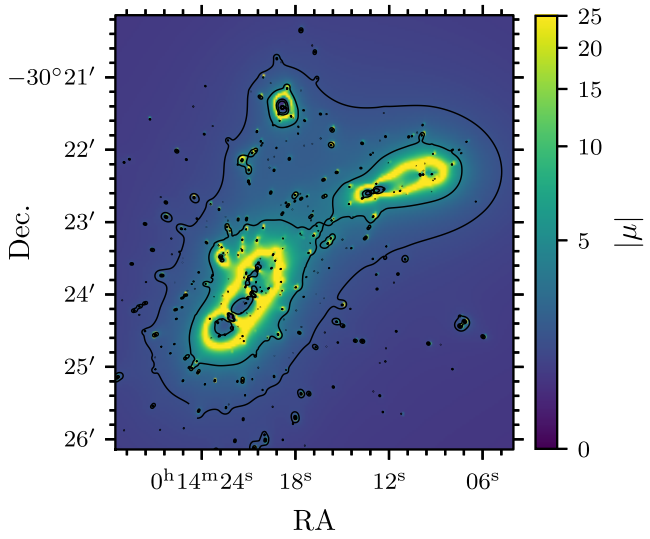

Figure 5. Magnification map of our final model for a source redshift $z_s = 10$. The black contours represent magnification thresholds of $\mu = 2$ and $\mu = 4$. The area between the main cluster and the extended sub-structures forms contiguous sheet of $\mu > 2$ which goes up to $\mu \gtrsim 4$ between the main cluster and the north-western extension.

2) than in both Mahler et al. (2018) and Bergamini et al. (2023) and even so, judging by the single multiply imaged system found around that clump (see Fig. 3), we suspect that the mass of this sub-structure is overestimated, as explained above.

The resulting parameters for the BCGs and cluster galaxies left free in our model (see Section 3.4) are listed in Table 3. We find the reference galaxy of (fixed) luminosity $M_\star = -21.05$ (in absolute magnitudes) to have a velocity dispersion $\sigma_{v,\star} = 117 \pm 4\ \frac{\mathrm{km}}{\mathrm{s}}$ and a truncation radius $r_{\mathrm{cut},\star} = 57 \pm 9$ kpc. The median scaling relations equations (4)–(6) are $\lambda = 0.40^{+0.02}_{-0.01}$, $\beta = 0.77^{+0.05}_{-0.02}$, and $\alpha = 0.63^{+0.01}_{-0.02}$. Note that these seem to work very well, as is evident by the fact that multiple image systems that lie very close to cluster galaxies, such that their lensing signal is dominated by them (e.g. systems 65 and 71; see Fig. 2), are exceptionally well reproduced by our model. In addition, the λ-parameter agrees perfectly with the value of $\simeq 0.4$ measured in Bergamini et al. (2023) from the internal stellar kinematics of cluster galaxies (Bergamini et al. 2019, 2021). While our result for the power-law index of the scaling relation for the truncation radius disagrees with the $\alpha \simeq 0.41$ kinematic measurement in Bergamini et al. (2023), we also find a much higher $r_{\mathrm{cut},\star}$ amplitude in our model despite our reference galaxy being fainter. Using equation (3), we compute the total mass of our reference galaxy $M_{\mathrm{tot},\star} = (5.7 \pm 1.8) \times 10^{11}\ \mathrm{M}_\odot$ which, together with its luminosity $L_\star = 2.2 \times 10^{10}\ \mathrm{L}_\odot$, agrees with typical halo mass to luminosity relations (e.g. Vale & Ostriker 2004). Finally, the median redshifts for the multiple image systems optimized in this model, i.e. all the new ones identified in UNCOVER imaging of the extended structures, are given in Table 1. Note that in the case of multiple image systems that split into several sub-systems, we report the median redshift of the best reproduced sub-system.

We make our SL model publicly available on the UNCOVER website under: https://jwst-uncover.github.io/DR1.html#LensingMaps. The release comprises 7.6 arcmin × 7.6 arcmin deflection maps, α_x and α_y, a convergence κ-map, and shear γ_1- and γ_2-maps, which cover the entire UNCOVER NIRCam footprint. We provide maps both in NIRCam UNCOVER pixel scale of 0.04 arcsec pix^{-1}, and in lower 0.1 arcsec pix^{-1} resolution for the best-fitting model and a range of low-resolution maps drawn from the final MCMC chain for error computation. The release also contains a set of magnification maps for various source redshifts.

The deep *JWST* imaging and SL mass model presented here for the first time fully reveal the SL power of the massive northern clumps (∼3 arcmin north and north-west of the main cluster core; see Fig. 4) in A2744. These were previously only constrained with WL measurements (Merten et al. 2011; Jauzac et al. 2016; Medezinski et al. 2016) which are much less sensitive to the small-scale mass distribution than the SL regime. While the WL analyses did indeed predict the three distinct northern sub-haloes that we also model, we are now able to pinpoint their exact positions due to the more sensitive SL signal (see Table 2) and can confirm the halo positions to coincide with the three BCG-type galaxies identified in the north of A2744 (see Section 3.2). Because of the different sensitivities of the SL and WL regimes, a direct quantitative comparison between the derived total masses is not possible. We nevertheless find the two northern sub-structures to be somewhat less massive than predicted by the WL, in particular by approximately one order of magnitude compared to Jauzac et al. (2016). Note that all three WL studies predict an additional massive sub-halo west of the cluster core (Merten et al. 2011; Jauzac et al. 2016; Medezinski et al. 2016), which lies just outside of the UNCOVER field of view. The extended *HST* data do not show a prominent cluster galaxy overdensity in that vicinity, even though there are two bright cluster galaxies at the position where Merten et al. (2011) predict the western sub-clump. We do not find any SL features in this region that could hint at an additional dense SL halo. That being said, the BUFFALO *HST* data in this region are

Table 2. Median DM halo PIEMD parameters, defined in equations (2) and (7) in Section 3.1, and their 1σ-errors for our SL model of A2744.

Halo	RA	Dec.	ϵ	θ [Degrees]	σ_v [$\frac{\mathrm{km}}{\mathrm{s}}$]	r_{core} [kpc]
			Main cluster core			
Main-1	$00{:}14{:}22.17^{+0.01}_{-0.01}$	$-30{:}24{:}18.32^{+0.31}_{-0.22}$	$0.41^{+0.02}_{-0.03}$	45^{+4}_{-1}	681^{+34}_{-16}	23^{+4}_{-2}
Main-2	$00{:}14{:}20.80^{+0.03}_{-0.01}$	$-30{:}24{:}00.85^{+0.29}_{-0.64}$	$0.45^{+0.01}_{-0.02}$	73^{+3}_{-2}	807^{+45}_{-72}	67^{+8}_{-20}
			North-western extension			
North-West−1	$00{:}14{:}13.16^{+0.02}_{-0.01}$	$-30{:}22{:}35.65^{+0.34}_{-0.13}$	$0.55^{+0.02}_{-0.02}$	19^{+3}_{-7}	407^{+21}_{-18}	5^{+1}_{-1}
North-West−2	$00{:}14{:}10.08^{+0.03}_{-0.01}$	$-30{:}22{:}19.90^{+0.22}_{-0.38}$	$0.18^{+0.02}_{-0.04}$	-8^{+3}_{-5}	906^{+30}_{-73}	62^{+4}_{-16}
			Northern extension			
North	00:14:18.83	−30:21:24.84	$0.10^{+0.02}_{-0.02}$	-73^{+2}_{-5}	486^{+17}_{-16}	2^{+2}_{-1}

Note. Column 1: DM halo designation; *Columns 2 and 3*: Right ascension and declination. The northern halo is fixed on to its BCG's position (see Section 3.4); *Column 4*: Ellipticity defined as $\epsilon = \frac{b-a}{a+b}$, where a and b are the semimajor and semiminor axes, respectively; *Column 5*: Position angle, counter-clockwise with respect to the east–west axis; *Column 6*: Velocity dispersion of the PIEMD profile; *Column 7*: Core radius of the PIEMD profile.

Table 3. Median dPIE parameters, defined in equations (1) and (2) in Section 3.1, and their 1σ-errors of the BCGs and the galaxies left free in our SL model of A2744.

Galaxy	RA[a]	Dec.[a]	σ_v [$\frac{\mathrm{km}}{\mathrm{s}}$]	r_{core} [kpc]	r_{cut} [kpc][b]	ϵ	θ [Degrees]	M_{tot} [10^{12} M$_\odot$]
				Main cluster core				
BCG1	00:14:22.09	−30:24:20.73	233^{+30}_{-15}	$0.525^{+0.033\ b}_{-0.016}$	126 ± 20	0.14 ± 0.02	31^{+3}_{-3}	$4.98^{+2.01}_{-1.67}$
BCG2	00:14:20.70	−30:24:00.59	311^{+26}_{-25}	$0.499^{+0.029\ b}_{-0.015}$	121 ± 19	0.09[a]	−67[a]	$8.52^{+3.00}_{-2.96}$
G1	00:14:22.75	−30:23:29.94	341^{+23}_{-19}	$0.469^{+0.026\ b}_{-0.013}$	115 ± 18	–	–	$9.73^{+3.27}_{-3.18}$
G2	00:14:20.49	−30:23:39.38	225^{+16}_{-22}	$0.364^{+0.014\ b}_{-0.007}$	94 ± 14	–	–	$3.44^{+1.16}_{-1.24}$
G3	00:14:21.03	−30:23:47.11	200^{+16}_{-16}	$0.326^{+0.010\ b}_{-0.005}$	86 ± 13	–	–	$2.48^{+0.86}_{-0.85}$
G4	00:14:22.20	−30:24:16.61	161^{+30}_{-16}	$0.287^{+0.007\ b}_{-0.003}$	77 ± 12	–	–	$1.45^{+0.70}_{-0.53}$
				North-western extension				
NW-BCG1	00:14:13.01	−30:22:34.72	$201^{+9\ b}_{-8}$	$0.562^{+0.037\ b}_{-0.019}$	134 ± 21	0.07[a]	38[a]	$3.92^{+1.26}_{-1.25}$
NW-BCG2	00:14:10.01	−30:22:20.79	218^{+18}_{-23}	$0.614^{+0.073}_{-0.050}$	126 ± 19	0.16 ± 0.01	-16^{+2}_{-6}	$4.36^{+1.52}_{-1.63}$
G5	00:14:09.81	−30:22:20.56	108^{+6}_{-7}	$0.095^{+0.007\ b}_{-0.003}$	31 ± 5	–	–	$0.27^{+0.09}_{-0.09}$
				Northern extension				
N-BCG	00:14:18.83	−30:21:24.83	$196^{+9\ b}_{-8}$	$0.533^{+0.034\ b}_{-0.017}$	128 ± 20	0.14[a]	−70[a]	$3.56^{+1.14}_{-1.14}$

Notes.[a] Fixed to the SEXTRACTOR-measured values (see Section 3.2).
[b] Scaled to the galaxy luminosity using the relations (4)–(6).
Note. *Column 1*: Galaxy designation; *Columns 2 and 3*: Right ascension and declination; *Column 4*: Velocity dispersion of the dPIE profile; *Column 5*: Core radius of the dPIE profile; *Column 6*: Truncation radius of the dPIE profile; *Column 7*: Ellipticity defined as $\epsilon = \frac{b-a}{a+b}$ where a and b are the semimajor and -minor axes respectively. All non-BCG-type galaxies are assumed to be spherical (see Section 3.1); *Column 8*: Position angle, counter-clockwise with respect to the east–west axis; *Column 9*: Total mass of the dPIE profile computed from the model parameters following equation (3).

shallower than the central HFF observations and possible faint SL features might therefore not be detected. Our model, however, does not require an external shear component (in early tries, introducing a freely optimized external shear free did not improve the model and the resulting external shear was very low), so if there is an additional sub-halo, it cannot be massive enough to significantly affect the SL signal of the multiple images identified in A2744 thus far. In addition, both Medezinski et al. (2016) and Jauzac et al. (2016) predict another sub-structure in the north-east of the main cluster but disagree on its position. The UNCOVER NIRCam data reveal a small overdensity of apparent cluster galaxies a few arcseconds from the Jauzac et al. (2016) predicted centroid which seems to contain one prominent candidate galaxy–galaxy SL system. There is not sufficient *HST* coverage of this region however to robustly select cluster galaxies. This feature is therefore not included in the present analysis because we select the cluster galaxies based on their colour around the 4000 Å-break in the *HST* data (see Section 3.2). Future analyses should nevertheless investigate this system with spectroscopy to see if an additional sub-halo is needed in the north-east of the cluster. The most prominent sub-structure in A2744 by far is the north-western extension as can be seen in Figs 2, 4, and 5. We note that its position and morphology align well with the cosmic filament direction found by Jauzac et al. (2016). Future studies combining both WL and SL modelling will be able to further examine these conclusions and expand on them. Given the wide field of view and unparalleled spatial resolution of the UNCOVER imaging, it will be particularly interesting to see how an UNCOVER-based WL analysis would agree or disagree with our SL-based findings.

The main limitation of our model is that, unlike the secure multiple images around the main cluster core (Bergamini et al. 2023), the newly discovered images around the two northern sub-structures do not have spectroscopic redshifts, which makes the SL model somewhat less secure in that region. Indeed, low numbers of spectroscopic redshift constraints have been found to strongly affect e.g. magnification measurements (e.g. Acebron et al. 2017, 2018; Meneghetti et al. 2017). However, the multitude of systems together with the relatively tightly constrained photometric redshifts for some of them (see Table 1) allow us to still obtain a relatively accurate solution as demonstrated by the low lens plane RMS achieved by our model. More robust modelling of these structures will however require spectroscopic redshift measurements of the new SL features detected in UNCOVER, either with VLT/MUSE for the brighter and bluer images or with *JWST*/NIRSpec for the fainter and redder ones such as our candidate $z \sim 2.5$ overdensity (see Section 3.3). The UNCOVER NIRSpec follow-up observations, scheduled for 2023 July, for example will be of great use in this regard.

The newly established SL sub-structure in the north of A2744 also now allows us to more precisely estimate the magnification of background sources in and around the cluster field since these have been found to be significantly affected by massive structures in the outskirts of simulated lensing clusters (e.g. Acebron et al. 2017; Meneghetti et al. 2017). Because of its unprecedented depth, large field of view, and numerous ancillary data sets (see Bezanson et al. 2022), the *JWST* UNCOVER field represents one of the prime fields for galaxy studies across the observable Universe. This is emphasized further by the relatively large high-magnification ($\mu \gtrsim 4$) area spanned by the cluster sub-structures, in particular the main cluster and the north-western extension (see Fig. 5), as discussed above. Studies of galaxies in this field will therefore require accurate gravitational magnification measurements such as provided by our SL model presented here and its subsequent versions.

5 CONCLUSION

We present a new parametric SL model of the galaxy cluster A2744 based on hitherto unknown multiple image systems in the northern and north-western extensions of the cluster. Due to the ultra-deep

and wide coverage of the *JWST*/NIRCam imaging taken for the UNCOVER program, we are able to identify numerous new multiple images and candidates in the two northern sub-structures of the cluster. Since no spectroscopic redshifts are available for these multiple image systems, we compile a relatively secure subset of SL constraints based on position, parity, and photometric redshifts, as well as support by preliminary lens models. These new SL constraints are then combined with the Bergamini et al. (2023) spectroscopic sample and a now confirmed $z_{\rm spec} = 9.76$ system (Roberts-Borsani et al. 2022) in the main cluster, forming a total sample of 135 multiple images used in our model. The SL model is constructed with an updated version of the parametric lensing mass modelling code by Zitrin et al. (2013a, b) and Zitrin (2021), and comprises five large-scale cluster DM haloes, five BCGs, and a total of 421 cluster galaxies. Our final model reproduces the multiple images with a *lens plane* RMS of 0.66 arcsec.

Our main results are the following:

(i) The UNCOVER imaging reveals two massive sub-structures ($\sim$3 arcmin) north and north-west of the central core of A2744. We uncover 75 new strongly lensed multiple images and multiple image candidates belonging to 17 sources around these structures, and establish them as prominent SL systems for the first time. These new multiple image systems include a potential overdensity of bright and red (i.e. *HST*-dark) sources at $z_{\rm phot} \sim 2.5$ behind the north-western sub-structure. We use 43 of these new multiple images to constrain our SL model in these regions.

(ii) Our model yields a total critical area of $A_{\rm crit} = 0.67\,{\rm arcmin}^2$ for A2744 (assuming a source redshift $z_{\rm s} = 2$) which implies an effective Einstein radius of $\theta_{\rm E} = 27.7 \pm 2.8$ arcsec enclosing a total projected mass of $M(< \theta_E) = (1.07 \pm 0.15) \times 10^{14}\,{\rm M}_{\odot}$. This corresponds to a total cluster mass of $M(r < 200\,{\rm kpc}) = (1.60 \pm 0.22) \times 10^{14}\,{\rm M}_{\odot}$ within 200 kpc of BCG2.

(iii) The main cluster core has an effective $z_{\rm s} = 2$ Einstein radius $\theta_{\rm E,\,main} = 23.2 \pm 2.3$ arcsec enclosing $M(< \theta_{E,{\rm main}}) = (7.7 \pm 1.1) \times 10^{13}\,{\rm M}_{\odot}$ and agrees well with previous SL models of A2744.

(iv) The northern and north-western sub-clumps have effective $z_{\rm s} = 2$ Einstein radii of $\theta_{\rm E,\,N} = 7.4 \pm 0.7$ arcsec and $\theta_{\rm E,\,NW} = 13.1 \pm 1.3$ arcsec, enclosing total masses of $M(< \theta_{E,{\rm N}}) = (0.8 \pm 0.1) \times 10^{13}\,{\rm M}_{\odot}$ and $M(< \theta_{E,{\rm NW}}) = (2.2 \pm 0.3) \times 10^{13}\,{\rm M}_{\odot}$, respectively. These substructures are somewhat less massive than in previous SL studies in which these DM sub-haloes were not directly constrained, however.

(v) Including the two northern sub-structures in the SL model effectively increased the critical area of the cluster by a factor $\sim$1.5. We in particular find an extended high-magnification (e.g. $\mu \gtrsim 4$ for $z_{\rm s} = 10$) area between the three cluster structures in the lens plane.

(vi) Our SL-constrained sub-structures broadly agree with WL analysis results of A2744 but find much lower masses for the individual DM haloes.

Our lens model is made available to the community, together with the public UNCOVER data release[5] (Bezanson et al. 2022). Future studies will need to measure spectroscopic redshifts of the newly discovered SL features in the outskirts of A2744 and include WL constraints to more robustly probe the complete DM sub-structure of the cluster. A part of that can be done with *JWST* UNCOVER data, including the upcoming NIRSpec spectroscopy. Our model will be updated in future versions with new constraints when they become available.

[5]https://jwst-uncover.github.io/DR1.html

ACKNOWLEDGEMENTS

We thank the anonymous referee for their useful comments and feedback that greatly helped to improve the completeness and clarity of this paper. LF and AZ would like to thank Ashish K. Meena for useful comments and discussions.

LF and AZ acknowledge support by Grant No. 2020750 from the United States-Israel Binational Science Foundation (BSF) and Grant No. 2109066 from the United States National Science Foundation (NSF). The BGU lensing group further acknowledges support by the Ministry of Science & Technology, Israel. HA acknowledges support from CNES (Centre National d'Etudes Spatiales). RB acknowledges support from the Research Corporation for Scientific Advancement (RCSA) Cottrell Scholar Award ID No.: 27587. PD acknowledges support from the NWO grant 016.VIDI.189.162 (ODIN) and from the European Commission's and University of Groningen's CO-FUND Rosalind Franklin program. The Cosmic Dawn Center is funded by the Danish National Research Foundation (DNRF) under grant #140. Support for the program JWST-GO-02561 was provided through a grant from the STScI under NASA contract NAS 5–03127.

This work is based on observations obtained with the NASA/ESA/CSA *JWST* and the NASA/ESA *Hubble Space Telescope (HST)*, retrieved from the `Barbara A. Mikulski Archive for Space Telescopes` (`MAST`) at the *Space Telescope Science Institute* (STScI). STScI is operated by the Association of Universities for Research in Astronomy, Inc. under NASA contract NAS 5–26555. This work is also based on observations made with ESO Telescopes at the La Silla Paranal Observatory which are publicly available on the ESO Science Archive Facility.

This research used `ASTROPY`,[6] a community-developed core Python package for Astronomy (Astropy Collaboration 2013; Price-Whelan et al. 2018) as well as the packages `NUMPY` (van der Walt, Colbert & Varoquaux 2011), `SCIPY` (Virtanen et al. 2020), `MATPLOTLIB` (Hunter 2007), and the `MAAT` Astronomy and Astrophysics tools for `MATLAB` (Ofek 2014).

DATA AVAILABILITY

The raw *JWST* and *HST* data used in this work are publicly available on the `MAST` and the reduced UNCOVER *JWST* and *HST* mosaics and catalogues are part of the public data release by the UNCOVER team[7] (Bezanson et al. 2022; Weaver et al. 2023). The spectroscopic redshifts were measured by Mahler et al. (2018), Bergamini et al. (2023) and Roberts-Borsani et al. (2022) based on data that are publicly available on the ESO Science Archive[8] and the GLASS website[9]

REFERENCES

Abell G. O., Corwin H. G., Jr., Olowin R. P., 1989, ApJS, 70, 1
Acebron A. et al., 2018, ApJ, 858, 42
Acebron A., Jullo E., Limousin M., Tilquin A., Giocoli C., Jauzac M., Mahler G., Richard J., 2017, MNRAS, 470, 1809
Allen S. W., 1998, MNRAS, 296, 392
Amoura Y., Drakos N. E., Berrouet A., Taylor J. E., 2021, MNRAS, 508, 100

[6]http://www.astropy.org
[7]https://jwst-uncover.github.io
[8]https://archive.eso.org/scienceportal/home
[9]https://glass.astro.ucla.edu

Asencio E., Banik I., Kroupa P., 2021, MNRAS, 500, 5249
Astropy Collaboration, 2013, A&A, 558, A33
Ata M., Lee K.-G., Vecchia C. D., Kitaura F.-S., Cucciati O., Lemaux B. C., Kashino D., Müller T., 2022, Nat. Astron., 6, 857
Atek H. et al., 2014, ApJ, 786, 60
Atek H. et al., 2015, ApJ, 800, 18
Atek H., Richard J., Kneib J.-P., Schaerer D., 2018, MNRAS, 479, 5184
Bacon R. et al., 2010, in McLean I. S., Ramsay S. K., Takami H.eds, Proc. SPIE Conf. Ser. Vol. 7735, Ground-based and Airborne Instrumentation for Astronomy III. SPIE, Bellingham, p. 773508
Barbary K., 2016, J. Open Source Softw., 1, 58
Barbary K., 2018, Astrophysics Source Code Library, record ascl: 1811.004
Barrufet L. et al., 2023, MNRAS, 522, 449
Bergamini P. et al., 2019, A&A, 631, A130
Bergamini P. et al., 2021, A&A, 645, A140
Bergamini P. et al., 2023, A&A, 670, A60
Bertin E., Arnouts S., 1996, A&AS, 117, 393
Bezanson R. et al., 2022, preprint (arXiv:2212.04026)
Bhatawdekar R., Conselice C. J., Margalef-Bentabol B., Duncan K., 2019, MNRAS, 486, 3805
Böker T. et al., 2023, PASP, 135, 038001
Borgani S., Guzzo L., 2001, Nature, 409, 39
Bouwens R. J., Illingworth G., Ellis R. S., Oesch P., Paulino-Afonso A., Ribeiro B., Stefanon M., 2022, ApJ, 931, 81
Bouwens R. J., Oesch P. A., Illingworth G. D., Ellis R. S., Stefanon M., 2017, ApJ, 843, 129
Braglia F. G., Pierini D., Biviano A., Boehringer H., 2009, A&A, 500, 947
Brammer G. B., van Dokkum P. G., Coppi P., 2008, ApJ, 686, 1503
Broadhurst T. J., Barkana R., 2008, MNRAS, 390, 1647
Broadhurst T., Umetsu K., Medezinski E., Oguri M., Rephaeli Y., 2008, ApJ, 685, L9
Caminha G. B., Suyu S. H., Mercurio A., Brammer G., Bergamini P., Acebron A., Vanzella E., 2022, A&A, 666, L9
Coe D. et al., 2019, ApJ, 884, 85
Coe D., Bradley L., Zitrin A., 2015, ApJ, 800, 84
de Lapparent V., Geller M. J., Huchra J. P., 1986, ApJ, 302, L1
Diego J. M. et al., 2023, A&A, 672, A3
Doyon R. et al., 2012, in Clampin M. C., Fazio G. G., MacEwen H. A., Oschmann Jacobus M. J., eds, Proc. SPIE Conf. Ser. Vol. 8442, Space Telescopes and Instrumentation 2012: Optical, Infrared, and Millimeter Wave.. SPIE, Bellingham, p. 84422R
Doyon R. et al., 2023, preprint (arXiv:2306.03277)
Dubois Y. et al., 2014, MNRAS, 444, 1453
Durret F. et al., 2016, A&A, 588, A69
Ebeling H., Barrett E., Donovan D., 2004, ApJ, 609, L49
Ebeling H., Barrett E., Donovan D., Ma C.-J., Edge A. C., van Speybroeck L., 2007, ApJ, 661, L33
Ebeling H., Edge A. C., Mantz A., Barrett E., Henry J. P., Ma C. J., van Speybroeck L., 2010, MNRAS, 407, 83
Elíasdóttir Á. et al., 2007, preprint (arXiv:0710.5636)
Ellien A., Durret F., Adami C., Martinet N., Lobo C., Jauzac M., 2019, A&A, 628, A34
Faber S. M., Jackson R. E., 1976, ApJ, 204, 668
Ferruit P. et al., 2022, A&A, 661, A81
Foley R. J. et al., 2011, ApJ, 731, 86
Fudamoto Y., Inoue A. K., Sugahara Y., 2022, ApJ, 938, L24
Furtak L. J. et al., 2022, preprint (arXiv:2212.10531)
Furtak L. J., Atek H., Lehnert M. D., Chevallard J., Charlot S., 2021, MNRAS, 501, 1568
Gardner J. P. et al., 2006, in Mather J. C., MacEwen H. A., de Graauw M. W. M., eds, Proc. SPIE Conf. Ser. Vol. 6265, Space Telescopes and Instrumentation I: Optical, Infrared, and Millimeter. SPIE, Bellingham, p. 62650N
Glazebrook K. et al., 2023, ApJ, 947, L25
González-López J. et al., 2017, A&A, 597, A41
Grillo C. et al., 2015, ApJ, 800, 38
Halkola A., Seitz S., Pannella M., 2006, MNRAS, 372, 1425
Halkola A., Seitz S., Pannella M., 2007, ApJ, 656, 739
Hatfield P. W., Laigle C., Jarvis M. J., Devriendt J., Davidzon I., Ilbert O., Pichon C., Dubois Y., 2019, MNRAS, 490, 5043
Hennawi J. F., Dalal N., Bode P., Ostriker J. P., 2007, ApJ, 654, 714
Hsiao T. Y.-Y. et al., 2022, preprint (arXiv:2210.14123)
Hunter J. D., 2007, Comput. Sci. Eng., 9, 90
Ishigaki M., Kawamata R., Ouchi M., Oguri M., Shimasaku K., Ono Y., 2015, ApJ, 799, 12
Ishigaki M., Kawamata R., Ouchi M., Oguri M., Shimasaku K., Ono Y., 2018, ApJ, 854, 73
Jaffe W., 1983, MNRAS, 202, 995
Jakobsen P. et al., 2022, A&A, 661, A80
Jauzac M. et al., 2012, MNRAS, 426, 3369
Jauzac M. et al., 2015, MNRAS, 452, 1437
Jauzac M. et al., 2016, MNRAS, 463, 3876
Jauzac M. et al., 2018, MNRAS, 481, 2901
Johnson T. L., Sharon K., 2016, ApJ, 832, 82
Johnson T. L., Sharon K., Bayliss M. B., Gladders M. D., Coe D., Ebeling H., 2014, ApJ, 797, 48
Jullo E., Kneib J.-P., 2009, MNRAS, 395, 1319
Jullo E., Kneib J.-P., Limousin M., Elíasdóttir Á., Marshall P. J., Verdugo T., 2007, New J. Phys., 9, 447
Kartaltepe J. S., Ebeling H., Ma C. J., Donovan D., 2008, MNRAS, 389, 1240
Kawamata R., Ishigaki M., Shimasaku K., Oguri M., Ouchi M., Tanigawa S., 2018, ApJ, 855, 4
Kawamata R., Oguri M., Ishigaki M., Shimasaku K., Ouchi M., 2016, ApJ, 819, 114
Keeton C. R., 2001, preprint (arXiv:astroph/0102341)
Keeton C. R., 2010, Gen. Relativ. Gravit., 42, 2151
Kelly P. L. et al., 2015, Science, 347, 1123
Kelly P. L. et al., 2016a, ApJ, 819, L8
Kelly P. L. et al., 2016b, ApJ, 831, 205
Kelly P. L. et al., 2018, Nat. Astron., 2, 334
Kikuchihara S. et al., 2020, ApJ, 893, 60
Kim J., Jee M. J., Perlmutter S., Hayden B., Rubin D., Huang X., Aldering G., Ko J., 2019, ApJ, 887, 76
Klypin A. A., Shandarin S. F., 1983, MNRAS, 204, 891
Kneib J. P., Mellier Y., Fort B., Mathez G., 1993, A&A, 273, 367
Kneib J.-P., Ellis R. S., Smail I., Couch W. J., Sharples R. M., 1996, ApJ, 471, 643
Kneib J.-P., Natarajan P., 2011, A&AR, 19, 47
Livermore R. C., Finkelstein S. L., Lotz J. M., 2017, ApJ, 835, 113
Lotz J. M. et al., 2017, ApJ, 837, 97
Mahler G. et al., 2018, MNRAS, 473, 663
Mahler G. et al., 2023, ApJ, 945, 49
Maizy A., Richard J., de Leo M. A., Pelló R., Kneib J. P., 2010, A&A, 509, A105
McElwain M. W. et al., 2023, PASP, 135, 058001
Medezinski E., Umetsu K., Okabe N., Nonino M., Molnar S., Massey R., Dupke R., Merten J., 2016, ApJ, 817, 24
Meena A. K. et al., 2023a, MNRAS, 521, 5224
Meena A. K. et al., 2023b, ApJ, 944, L6
Meneghetti M. et al., 2017, MNRAS, 472, 3177
Meneghetti M., Bartelmann M., Jenkins A., Frenk C., 2007a, MNRAS, 381, 171
Meneghetti M., Argazzi R., Pace F., Moscardini L., Dolag K., Bartelmann M., Li G., Oguri M., 2007b, A&A, 461, 25
Meneghetti M., Bartelmann M., Moscardini L., 2003, MNRAS, 340, 105
Merten J. et al., 2011, MNRAS, 417, 333
Miller T. B. et al., 2018, Nature, 556, 469
Monna A. et al., 2014, MNRAS, 438, 1417
Monna A. et al., 2015, MNRAS, 447, 1224
Mullis C. R., Rosati P., Lamer G., Böhringer H., Schwope A., Schuecker P., Fassbender R., 2005, ApJ, 623, L85
Naidu R. P. et al., 2022, preprint (arXiv:2208.02794)
Nelson E. J. et al., 2023, ApJ, 948, L18
Nonino M. et al., 2023, ApJ, 942, L29
Ofek E. O., 2014, Astrophysics Source Code Library, record ascl: 1407.005

Oguri M., Bayliss M. B., Dahle H., Sharon K., Gladders M. D., Natarajan P., Hennawi J. F., Koester B. P., 2012, MNRAS, 420, 3213
Oguri M., Takada M., Okabe N., Smith G. P., 2010, MNRAS, 405, 2215
Okabe N., Okura Y., Futamase T., 2010, ApJ, 713, 291
Oke J. B., Gunn J. E., 1983, ApJ, 266, 713
Owers M. S., Randall S. W., Nulsen P. E. J., Couch W. J., David L. P., Kempner J. C., 2011, ApJ, 728, 27
Pascale M. et al., 2022, ApJ, 938, L6
Price-Whelan A. M. et al., 2018, AJ, 156, 123
Priewe J., Williams L. L. R., Liesenborgs J., Coe D., Rodney S. A., 2017, MNRAS, 465, 1030
Redlich M., Bartelmann M., Waizmann J. C., Fedeli C., 2012, A&A, 547, A66
Richard J. et al., 2014, MNRAS, 444, 268
Richard J. et al., 2021, A&A, 646, A83
Rieke M. J. et al., 2023, PASP, 135, 028001
Roberts-Borsani G. et al., 2022, preprint (arXiv:2210.15639)
Rodney S. A. et al., 2015, ApJ, 811, 70
Rodney S. A., Brammer G. B., Pierel J. D. R., Richard J., Toft S., O'Connor K. F., Akhshik M., Whitaker K. E., 2021, Nat. Astron., 5, 1118
Sereno M., Jetzer P., Lubini M., 2010, MNRAS, 403, 2077
Sharon K., Gladders M. D., Rigby J. R., Wuyts E., Koester B. P., Bayliss M. B., Barrientos L. F., 2012, ApJ, 746, 161
Springel V. et al., 2005, Nature, 435, 629
Stanford S. A. et al., 2012, ApJ, 753, 164
Steinhardt C. L. et al., 2020, ApJS, 247, 64
Strait V. et al., 2020, ApJ, 888, 124
Strait V. et al., 2021, ApJ, 910, 135
Torri E., Meneghetti M., Bartelmann M., Moscardini L., Rasia E., Tormen G., 2004, MNRAS, 349, 476
Treu T. et al., 2015, ApJ, 812, 114
Treu T. et al., 2022, ApJ, 935, 110
Tully R. B., Fisher J. R., 1977, A&A, 54, 661
Vale A., Ostriker J. P., 2004, MNRAS, 353, 189
van der Walt S., Colbert S. C., Varoquaux G., 2011, Comput. Sci. Eng., 13, 22
Virtanen P. et al., 2020, Nat. Methods, 17, 261
Wallington S., Narayan R., 1993, ApJ, 403, 517
Wang T. et al., 2016, ApJ, 828, 56
Wang X. et al., 2015, ApJ, 811, 29
Weaver J. R. et al., 2023, preprint (arXiv:2301.02671)
Welch B. et al., 2022, Nature, 603, 815
Williams H. et al., 2023, Science, 380, 416
Zavala J. A. et al., 2023, ApJ, 943, L9
Zeldovich I. B., Einasto J., Shandarin S. F., 1982, Nature, 300, 407
Zheng W. et al., 2014, ApJ, 795, 93
Zitrin A. et al., 2009, MNRAS, 396, 1985
Zitrin A. et al., 2013a, ApJ, 762, L30
Zitrin A., Menanteau F., Hughes J. P., Coe D., Barrientos L. F., Infante L., Mandelbaum R., 2013b, ApJ, 770, L15
Zitrin A. et al., 2014, ApJ, 793, L12
Zitrin A. et al., 2015, ApJ, 801, 44
Zitrin A., 2021, ApJ, 919, 54

SUPPORTING INFORMATION

Supplementary data are available at *MNRAS* online.

Please note: Oxford University Press is not responsible for the content or functionality of any supporting materials supplied by the authors. Any queries (other than missing material) should be directed to the corresponding author for the article.

[1]*Physics Department, Ben-Gurion University of the Negev, P.O. Box 653, BeÃ¢Â€Â™er-Sheva 84105, Israel*
[2]*Department of Astronomy, University of Massachusetts, Amherst, MA 01003, USA*
[3]*Institut d'Astrophysique de Paris, CNRS, Sorbonne Université, 98bis Boulevard Arago, F-75014 Paris, France*
[4]*Department of Physics and Astronomy and PITT PACC, University of Pittsburgh, Pittsburgh, PA 15260, USA*
[5]*Centre for Astrophysics and Supercomputing, Swinburne University of Technology, Melbourne, VIC 3122, Australia*
[6]*Department of Astronomy & Astrophysics, The Pennsylvania State University, University Park, PA 16802, USA*
[7]*Institute for Computational & Data Sciences, The Pennsylvania State University, University Park, PA 16802, USA*
[8]*Institute for Gravitation and the Cosmos, The Pennsylvania State University, University Park, PA 16802, USA*
[9]*Cosmic Dawn Center (DAWN), Niels Bohr Institute, University of Copenhagen, Jagtvej 128, DK-2200 København N, Denmark*
[10]*Department of Physics and Astronomy, Tufts University, 574 Boston Ave., Medford, MA 02155, USA*
[11]*Kapteyn Astronomical Institute, University of Groningen, P.O. Box 800, NL-9700 AV Groningen, the Netherlands*
[12]*Department of Astronomy, Yale University, New Haven, CT 06511, USA*
[13]*Institute for Computational Science, University of Zurich, Winterhurerstrasse 190, CH-8006 Zurich, Switzerland*
[14]*Department of Astronomy, The University of Texas at Austin, Austin, TX 78712, USA*
[15]*Leiden Observatory, Leiden University, P.O. Box 9513, NL-2100 RA Leiden, the Netherlands*
[16]*Department for Astrophysical and Planetary Science, University of Colorado, Boulder, CO 80309, USA*
[17]*Dunlap Institute for Astronomy and Astrophysics, 50 St George Street, Toronto, ON M5S 3H4, Canada*

This paper has been typeset from a TEX/LATEX file prepared by the author.